

Ring-Slippage and Multielectron Redox Properties of Fe/Ru/Os–Bis(arene) Complexes: Does Hapticity Change Really Cause Potential Inversion?

Richard L. Lord,[†] Cynthia K. Schauer,[§] Franklin A. Schultz,^{†,‡} and Mu-Hyun Baik^{*,†,#}

[†]Department of Chemistry, Indiana University, 800 East Kirkwood Avenue, Bloomington, Indiana 47405, United States

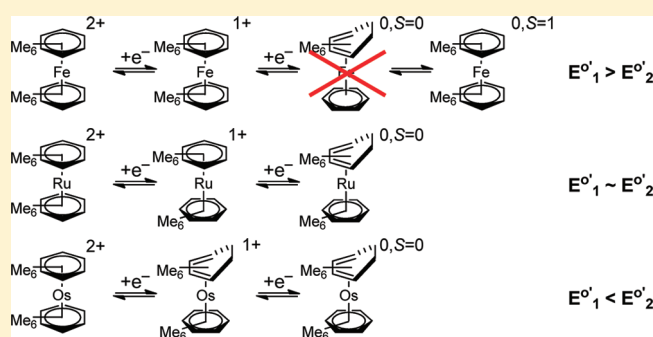
[‡]Department of Chemistry and Chemical Biology, Indiana University Purdue University Indianapolis, 402 North Blackford Street, Indianapolis, Indiana 46202, United States

[§]Department of Chemistry, University of North Carolina, Chapel Hill, North Carolina 27599, United States

[#]Department of Chemistry, Korea University, 208 Seochang, Chochiwon, Chung-nam 339-700, South Korea

S Supporting Information

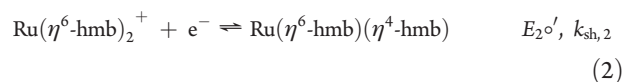
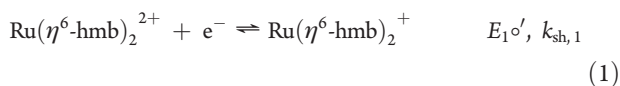
ABSTRACT: Bis(hexamethylbenzene) complexes of the group 8 metals (Fe, Ru, Os) show surprising diversity in their electron-transfer mechanisms and associated thermodynamics for the $M^{II} \rightarrow M^I \rightarrow M^0$ redox series. In electrochemical experiments, the Fe complex exhibits normally ordered potentials separated by ~ 1 V, the Ru system shows nearly overlapping one-electron redox events, and Os demonstrates a one-step, two-electron transfer with a peak potential separation suggestive of highly inverted potentials. It has been conjectured that the sequential one-electron transfers observed for Fe are due to the lack of an accessible $\eta^4:\eta^6$ Fe^0 state, destabilizing the fully reduced species. Using an established model chemistry based on DFT, we demonstrate that the hapticity change is a consequence of the bonding throughout this transition metal triad and that apparent multielectron behavior is controlled by the vertical electron attachment component of the $M^{II} \rightarrow M^I$ redox event. Furthermore, the $\eta^6:\eta^6$ Fe^0 triplet state is more favorable than the hypothetical $\eta^4:\eta^6$ singlet state, emphasizing that the hapticity change is not sufficient for multielectron behavior. Despite both displaying two-electron redox responses, Ru and Os traverse fundamentally different mechanisms based on whether the first (Os) or second (Ru) electron transfer induces the hapticity change. While the electronic structure analysis is limited to the Fe triad here, the conceptual model that we developed provides a general understanding of the redox behavior exhibited by d^6 bis(arene) compounds.



INTRODUCTION

Transition metal–bis(arene) complexes constitute one paradigm of the widespread and highly utilitarian sandwich compounds. As such they find application in many areas of practical interest including synthesis, catalysis, materials science, and biomedicine.^{1–8} A notable property of the group 8–bis(hexamethylbenzene) complexes is the reversible $\eta^6 \rightarrow \eta^4$ hapticity change of one coordinated arene ring which accompanies two-electron transfer—a reaction that dramatically alters the electronic properties of the metal and ring and can lead to useful chemical reactivity.

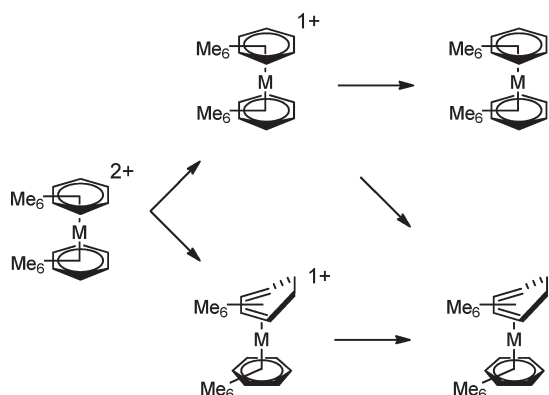
The prototypical example is the widely studied $Ru(hmb)_2^{2+/+ / 0}$ (hmb = hexamethylbenzene) redox system,^{9–11} which reacts via two one-electron transfers at closely overlapping ($E_1^{o'} \approx E_2^{o'}$) or slightly inverted ($E_1^{o'} < E_2^{o'}$) potentials.



Although the thermodynamics of reactions 1 and 2 are slightly inverted in acetonitrile ($\Delta E^{o'} = E_2^{o'} - E_1^{o'} = +30$ mV), the second electron transfer is much slower than the first (i.e., $k_{sh,2} \ll k_{sh,1}$), and the individual steps can be resolved kinetically by fast scan cyclic voltammetry.^{10,11} This observation is consistent with the interpretation that the hapticity change (conveying greater nuclear reorganization) accompanies addition of the second electron and provides the driving force for apparent transfer of two electrons in a single step. In contrast, the $Fe(hmb)_2^{2+}$ congener exhibits normally ordered potentials separated by 1.2 V, with the Fe^+ and Fe^0 states retaining η^6 binding of both arene rings.¹² The electrochemistry of $Os(hmb)_2^{2+}$, although less thoroughly investigated,^{13,14} shows two equivalents of charge

Received: June 8, 2011

Published: September 06, 2011

Scheme 1. Mechanistic Possibilities for the First and Second Reductions of Bis(hexamethylbenzene) Complexes

Table 1. Thermodynamic Parameters for $[M(\text{hmb})_2]^{2+/+0}$ Redox Couples

metal	experimental conditions	$E^{o'}$, ^a V vs Fc/Fc ⁺	$\Delta E^{o'}$, V	ref
Fe (1)	CH ₃ CN, 0.1 M Bu ₄ NPF ₆	-0.67, -1.87	-1.20	12
Ru (2)	CH ₃ CN, 0.5 M Bu ₄ NPF ₆	-1.41	+0.03	10,11
Os (3)	CH ₃ CN, 0.15 M Bu ₄ NPF ₆	-1.3	$\gg 0$	13

^a Measured as the average of cathodic and anodic peak potentials by cyclic voltammetry.

to be transferred in a single step based on peak current magnitudes. However, little mechanistic insight can be gleaned, because the large voltammetric peak potential separation ($\Delta E_p = 500\text{--}700\text{ mV}$) suggests significant potential inversion and highly irreversible electron-transfer kinetics,¹⁵ and neither the mono-cation nor the neutral form has been isolated or characterized *in situ*. Scheme 1 outlines the various mechanistic possibilities for timing of the hapticity change and electron transfer in these group 8 systems, and their known thermodynamics are summarized in Table 1. The possible existence of alternative spin states for the fully reduced species is not noted but will be considered subsequently.

Certain mixed-sandwich and half-sandwich arene complexes also exhibit an electron-transfer-initiated $\eta^6 \rightarrow \eta^4$ hapticity change, leading to apparent multielectron transfer and a congeneric pattern of behavior similar to that found for $M(\text{hmb})_2^{2+/+0}$. One such example is the $M(\text{Cp}^*)(\text{hmb})^{2+/+0}$ ($M = \text{Co}, \text{Rh}, \text{Ir}$; $\text{Cp}^* =$ pentamethylcyclopentadiene) family of compounds. $\text{Co}(\text{Cp}^*)(\text{hmb})^{2+}$ undergoes normally ordered one-electron reductions separated by $\sim 1\text{ V}$,¹⁶ whereas $\text{Ir}(\text{Cp}^*)(\text{hmb})^{2+}$ undergoes kinetically irreversible two-electron reduction in a single step with potential inversion estimated to be $+250\text{--}320\text{ mV}$.¹⁷ $\text{Rh}(\text{Cp}^*)(\text{hmb})^{2+}$ is reduced sequentially in two noninverted, closely spaced one-electron transfers ($\Delta E^{o'} = -90$ to -370 mV).¹⁸ It has been established that the arene ring retains planarity in the Rh(II) intermediate and that the hapticity change and sluggish electron transfer coincide in the second step.^{19,20} A further example occurs among group 7 mono(arene) complexes, where $(\eta^6\text{-C}_6\text{Me}_6)\text{Re}(\text{CO})_3^+$ is reduced in a chemically reversible two-electron reaction to the η^4 ring-slipped product with $\Delta E^{o'} \cong +500\text{ mV}$ and $k_{\text{sh},2} \ll k_{\text{sh},1}$, whereas $(\eta^6\text{-C}_6\text{Me}_6)\text{Mn}(\text{CO})_3^+$

undergoes one-electron reduction to a highly reactive product at room temperature.²¹

Over the past decade, our laboratories have sought a fundamental understanding of the molecular features governing multi-electron transfer through computational studies of selected redox systems.^{22–27} The bis(hmb) complexes of Fe, Ru, and Os are appealing targets in this regard, because they exhibit electrochemical responses ranging from normally ordered potentials (Fe), to nearly overlapping one-electron reactions (Ru), and to a highly inverted two-electron transfer (Os). Detailed examination of the underlying causes of this behavior will provide useful insight not only to $M(\text{hmb})_2^{2+/+0}$ redox chemistry but also to similar reactivity exhibited by other transition metal sandwich compounds possessing d^6 , d^7 , and d^8 configurations.

As detailed in our earlier studies,^{22–27} potential inversion and its multielectron outcome require the second step in an electron-transfer chain (e.g., reaction 2) be thermodynamically more favorable than the first (reaction 1).^{28–30} The energetics of these processes are readily calculated by density functional theory in combination with a continuum solvation model.³¹ Whereas solvation and often ion-pairing are important contributors to the overall energy change of charge-transfer reactions, important differences arise from internal molecular energies for a homologous series of compounds. Thus, we have devised a protocol for dissecting the free energies of reduction into vertical electron attachment and structural relaxation components by means of a theoretical square scheme,²³ where the former refers to the energy of adding a free electron to the molecule without allowing the atoms to change position. Thus, the electron attachment energy is the negative of electron affinity and is used here to be sign-consistent with the definition of redox potentials and chemically intuitive in that exergonic processes are associated with negative energies. Outwardly, a major structural change such as a haptotropic rearrangement is suspect for providing the necessary driving force for potential inversion. The electron attachment energies are, however, much greater in magnitude than those associated with nuclear reorganization, and comprehensive electronic structure analysis is needed to reach a fundamental understanding of the origins of potential inversion, as emphasized in a recent investigation.²⁷ Below we present an in-depth computational study of the electron-transfer and ring-slip reactions of group 8–bis(hexamethylbenzene) complexes with the goal of achieving a better understanding of this prevalent reaction in transition metal–arene chemistry and for designing future multielectron catalysts.

COMPUTATIONAL DETAILS

Geometry optimizations and the evaluation of thermochemical properties were completed using density functional theory as implemented in the Jaguar 7.0 suite of quantum chemistry programs.³² Geometry optimizations were performed at the B3LYP*/6-31G** level of theory, with Fe, Ru, and Os represented using the Los Alamos LACVP basis set.^{33–42} This model chemistry was found to generate reasonable structures but unsatisfactory electronic energies for redox phenomena.^{31,42} Subsequent single-point calculations were thus conducted with Dunning's correlation-consistent triple- ζ basis set cc-pVTZ(-f) for main-group elements and a decontracted version of LACVP to match the effective core potential with a triple- ζ -quality basis for Fe, Ru, and Os.⁴⁴ Solvation energies were computed at the double- ζ level using a self-consistent reaction field approach based on numerical solutions of the Poisson–Boltzmann equation, computed at the optimized gas-phase geometry utilizing an appropriate dielectric

Table 2. Computed Thermodynamics of Electron Transfer and Disproportionation for 1–3

reaction	$\Delta G(\text{gas}), \text{eV}$	$\Delta\Delta G_{\text{solv}}, \text{eV}$	$\Delta G(\text{sol}), \text{eV}$	$E_{\text{comp}}^{\circ}, \text{V vs Fc/Fc}^{+}$	$E_{\text{obs}}^{\circ}, \text{V vs Fc/Fc}^{+}$
$1^{2+} + e^{-} \rightarrow 1^{+}$	-8.676	4.556	-4.120	-0.675	-0.67
$1^{+} + e^{-} \rightarrow 1^{0,T}$	-4.608	1.501	-3.106	-1.689	-1.87
$1^{2+} + 2e^{-} \rightarrow 1^{0,T}$	-13.284	6.058	-7.226	-1.182	–
$21^{+} \rightarrow 1^{2+} + 1^{0,T}$	4.069	-3.055	1.014	-1.014	-1.20
$2^{2+} + e^{-} \rightarrow 2^{+}$	-7.749	4.502	-3.248	-1.547	–
$2^{+} + e^{-} \rightarrow 2^{0}$	-4.650	1.466	-3.184	-1.611	–
$2^{2+} + 2e^{-} \rightarrow 2^{0}$	-12.399	5.968	-6.431	-1.579	-1.41
$22^{+} \rightarrow 2^{2+} + 2^{0}$	3.100	-3.035	0.064	-0.064	0.03
$3^{2+} + e^{-} \rightarrow 3^{+}$	-7.552	4.496	-3.055	-1.740	–
$3^{+} + e^{-} \rightarrow 3^{0}$	-4.944	1.452	-3.493	-1.302	–
$3^{2+} + 2e^{-} \rightarrow 3^{0}$	-12.496	5.948	-6.548	-1.521	-1.3
$23^{+} \rightarrow 3^{2+} + 3^{0}$	2.607	-3.045	-0.437	0.437	$\gg 0$

constant for comparison to the experimental conditions ($\epsilon = 37.5$ for acetonitrile).^{45,46} The standard set of optimized radii in Jaguar were employed: Fe, 1.456 Å; Ru, 1.481 Å; Os, 1.560 Å; H, 1.150 Å; C, 1.900 Å.⁴⁷ Vibrational analyses using analytical frequencies also were computed at the double- ζ level, ensuring all stationary points to be minima. Differential entropies derived from these calculations were unusually large due to the overweight that low-energy vibrations associated with rotational and angle distortion modes of the methyl groups receive in a standard harmonic oscillator-based treatment of the vibrational partition function. This intrinsic problem gives rise to unreliable entropy differences that are difficult to eliminate properly and overshadow the physically meaningful entropy differentials due to the hapticity change. As a reasonable compromise we used $S(\text{gas})$ differential values derived from small (bis-benzene) models that capture the latter entropy change appropriately, while not suffering from the spurious vibrational modes of the methyl groups that decorate the arene ring (see Supporting Information). Differences in thermodynamic properties were obtained as shown in eqs 3–7, with standard approximations assumed for gas-phase entropy corrections using unscaled frequencies.⁴⁸

$$\Delta H(\text{gas}) = \Delta E(\text{SCF}) + \Delta ZPE \quad (3)$$

$$\Delta G(\text{gas}) = \Delta H(\text{gas}) - 298.15 \text{ K } \Delta S(\text{gas}) \quad (4)$$

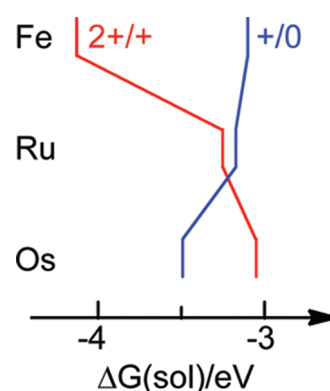
$$\Delta G(\text{sol}) = \Delta G(\text{gas}) + \Delta\Delta G_{\text{solv}} \quad (5)$$

$$\Delta G^{\text{EA}}(\text{sol}) = -nFE_{\text{comp,abs}}^{\circ} \quad (6)$$

$$E_{\text{comp}}^{\circ} = E_{\text{comp,abs}}^{\circ} - 4.795 \text{ V} \quad (7)$$

where $\Delta H(\text{gas})$ is the gas-phase enthalpy change, $\Delta E(\text{SCF})$ is the electronic energy change, ΔZPE is the zero-point energy correction difference, $\Delta G(\text{gas})$ is the gas-phase Gibbs free energy change, $\Delta S(\text{gas})$ is the gas-phase entropy change, $\Delta G(\text{sol})$ is the solution-phase free energy change, $\Delta\Delta G_{\text{solv}}$ is the differential free energy of solvation, $\Delta G^{\text{EA}}(\text{sol})$ is the solvated free energy change of reduction, $E_{\text{comp,abs}}^{\circ}$ is the absolute standard reduction potential, and E_{comp}° is the standard reduction potential vs Fc/Fc⁺. Absolute potentials were converted to values relative to Fc/Fc⁺ by use of eq 7. The 4.795 V correction term differs slightly from the absolute ferrocene potential of 4.978 V employed previously by our group^{24–27} and, following upon the recent suggestion of Batista,⁴⁸ includes an empirically established offset of 183 mV determined by fitting B3LYP*-calculated potentials to experimental values using a set of redox systems not reported here.⁴⁹

Scheme 2



RESULTS AND DISCUSSION

Redox Potentials and Disproportionation Free Energies.

The thermodynamics of the one- and two-electron-transfer reactions and disproportionation free energies of 1–3 are enumerated in Table 2 and visualized in Scheme 2.⁵⁰ The solution-phase free energy $\Delta G(\text{sol})$ for each disproportionation reaction corresponds to the extent of potential inversion ΔE° , differing only in sign (eq 6). Our model chemistry accurately predicts the experimental potentials for all three systems, with errors ranging from <10 mV for the first Fe reduction to 0.2 V for Os. The latter error is slightly larger than typically observed³¹ and possibly results from the large, scan-rate-dependent peak potential separation of the Os(hmb)₂^{2+/0} system,¹³ which leads to a relatively large uncertainty in the experimentally determined potential. Interestingly, our calculations reveal a large increase in the extent of potential inversion upon descending the periodic table, illustrated in Scheme 2 by the inversion of ordering of $\Delta G(\text{sol})$. The first and second potentials are ordered normally by 1.014 V for Fe (1), which compares well with the 1.20 V separation observed by Kochi.¹² For Ru (2) our calculations give reduction potentials of -1.547 and -1.611 V, respectively. Thus, the computed potential difference is -0.064 V, and they are formally predicted to not be inverted; i.e., the second potential is more negative than the first. Experimentally, the potential inversion has been estimated to be ~0.03 V in acetonitrile, with the extent of potential inversion being solvent dependent.^{10,11} A more substantial potential inversion of 437 mV

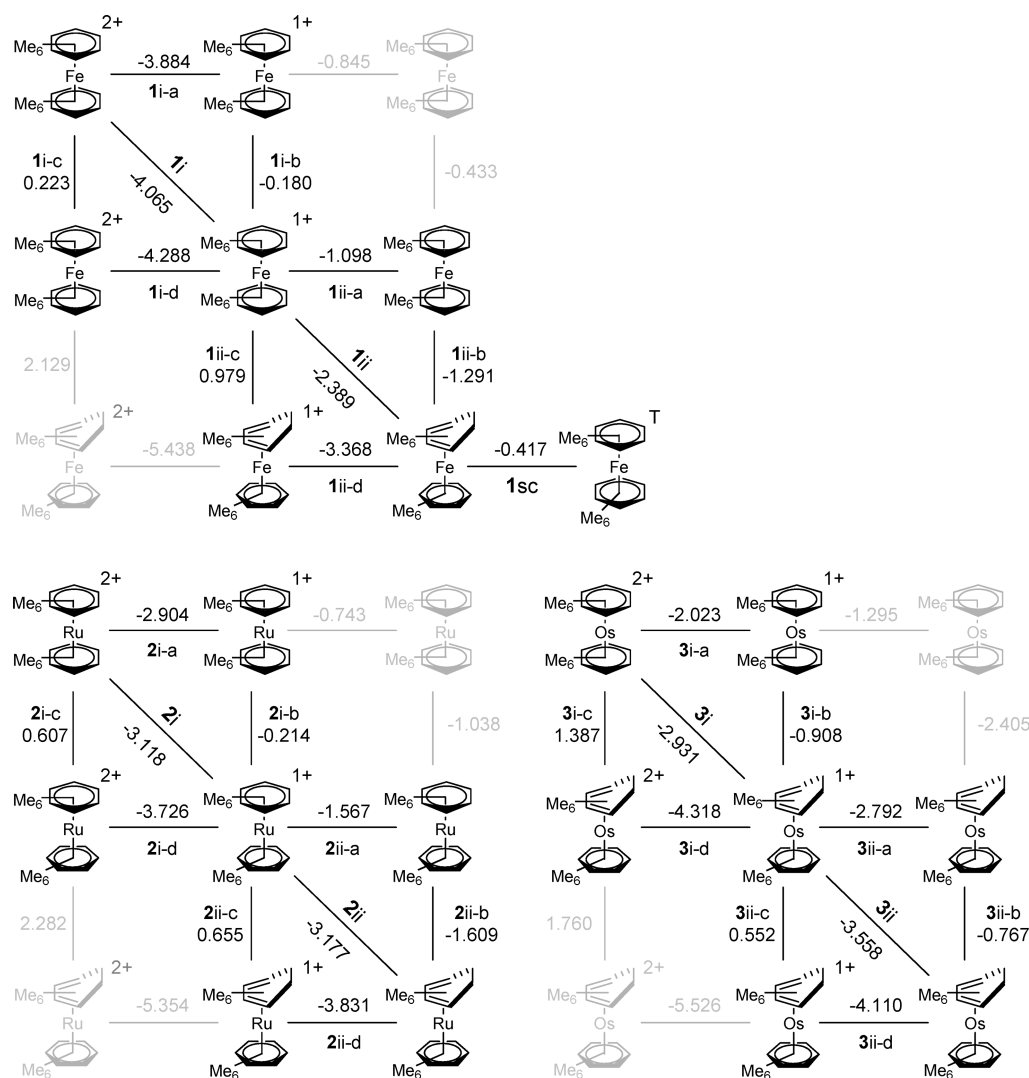


Figure 1. Theoretical square schemes for 1–3. The horizontal direction corresponds to vertical electron transfer; the vertical direction corresponds to structural change. $\Delta G(\text{sol})'$ values are in eV.

is predicted for Os (3). Although no quantitative measurement of ΔE^{red} is available for the Os system, the calculated value is consistent with the observed experimental behavior.^{13,15} In conclusion, the model chemistry we constructed successfully reproduces the electron-transfer thermodynamics of 1–3, illustrating the dramatically different redox behavior going from Fe \rightarrow Ru \rightarrow Os and justifying a more detailed analysis of the underlying electronic structure to identify the features that lead to this remarkable, apparently consistent redox behavior. One possible origin of potential inversion that has often been speculated upon is differential solvation of the two redox events: For 1–3, it is plausible that the 2+ \rightarrow 1+ reduction may require unusually large energy relative to the 1+ \rightarrow 0 step, as the first reduction must be associated with a much greater solvation energy loss than the second. This asymmetric distribution of solvation energy loss will conceptually make the first step more difficult, i.e., decrease the energy difference between the two redox pairs, whereas the second will become easier, as the thermodynamic driving force will be increased more significantly by solvation compared to the first redox pair. For each system, however, the differential solvation energy for the first reduction

($\Delta\Delta G_{\text{solv},i}$) is less than 2² times that of the second ($\Delta\Delta G_{\text{solv},ii}$), as predicted by Born model analysis. Furthermore, the $\Delta\Delta G_{\text{solv}}$ values are effectively metal and spin-state independent ($\Delta\Delta G_{\text{solv},i} \approx 4.5$ eV, $\Delta\Delta G_{\text{solv},ii} \approx 1.5$ eV), which is inconsistent with the differing extents of potential inversion down the period. Thus, whereas the differential solvation energy is conceptually intuitive, we concluded that it is not the main source of potential inversion in this system. Instead, we show below that the source of the potential inversion differences lies in the electronic and/or geometric structures of these species.

Theoretical Square Schemes. As we demonstrated previously,^{22–27} electrochemically inspired theoretical square schemes (Figure 1) allow for separation of energetic changes due to electron attachment and structural relaxation in a chemically meaningful manner. Here, electrons are added along the horizontal lines of the diagram while maintaining a constant structure. Structural changes occur along the vertical lines of the diagram within a constant redox state. Values along the diagonal are adiabatic electron attachment energies that are comparable directly to experimental redox potentials and for which $\Delta G(\text{sol})'$ can be computed. The off-diagonal states, however, are not

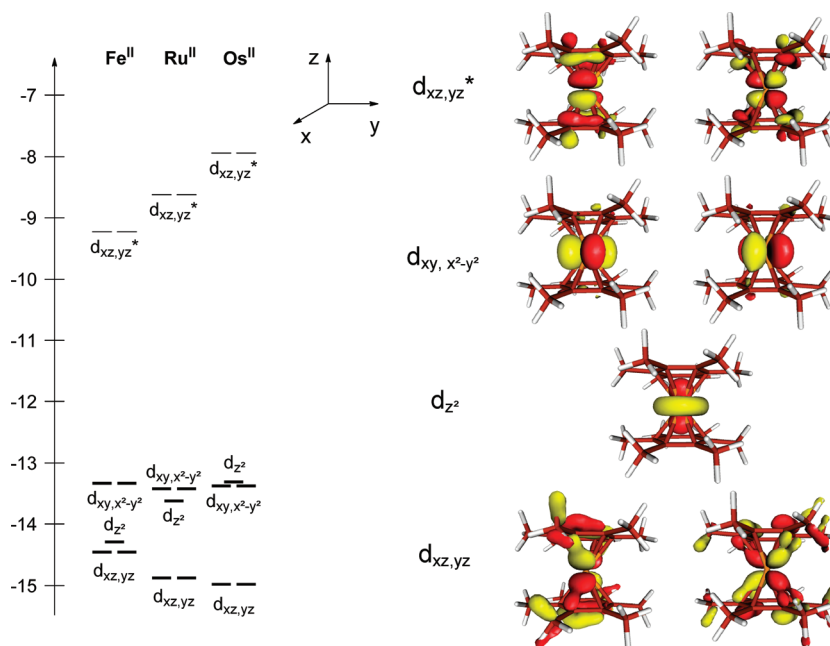


Figure 2. Frontier orbital energy diagram (in eV) for $M(\text{hmb})_2^{2+}$ species. Occupied and vacant orbitals are represented by bold and regular lines, respectively. Representative plots for $\text{Ru}(\text{hmb})_2^{2+}$ are shown.

minima on their respective potential energy surfaces, and the harmonic approximation used to derive thermodynamic corrections is no longer valid. Thus, an approximate solution-phase free energy, $\Delta G(\text{sol})' = \Delta E(\text{SCF}) + \Delta \Delta G_{\text{solvr}}$, is introduced for the purpose of comparison. Whereas this procedure leads to slightly different numbers, the salient features of the relative energies are faithfully maintained. For the purpose of understanding the redox chemistry, $\Delta G(\text{sol})'$ and $\Delta G(\text{sol})$ can be exchanged without loss of any significant meaning.⁵¹ Theoretical square schemes for **1–3** are found in Figure 1, with the most relevant steps labeled for ease of reference. To maintain consistency of comparison throughout the series, the singlet Fe^0 species is included in addition to the experimentally observed triplet, and the spin-crossover energy is incorporated into the diagram.

It is instructive first to examine the qualitative structural changes, and consequently the different mechanisms, for each species. All three compounds begin as dications in a pseudo- D_{6h} conformation with both arene rings bound η^6 to the metal center. Reduction by one electron affords a 19-electron M^I intermediate for Fe and Ru with both arenes η^6 -bound. However, formation of $[\text{Os}(\text{hmb})_2]^+$ is accompanied by an $\eta^6 \rightarrow \eta^4$ hapticity change of one arene ring, which bends by 34° . Thus, the Os system follows a qualitatively different two-electron-transfer pathway via a 17-electron intermediate, whose favorable reduction is an integral component of the large potential inversion. The second electron transfer to Fe and Ru induces a hexa- to tetrahapto shift of one hexamethylbenzene, with the amount of arene bending increasing down the triad (42.6° , 46.5° , and 50.2° for Fe, Ru, and Os, respectively). This hapticity change coincides with formation of the singlet M^0 states that have been enforced computationally to investigate periodic trends and is a consequence of double occupation of either the d_{xz} or d_{yz} orbital of the degenerate M –hmb antibonding pair (*vide infra*). As is frequently the case for first-row transition metals, the high-spin triplet state of Fe is favored by 0.417 eV (I_{SC}). Because the triplet contains one electron in each of the antibonding orbitals, hapticity change is

unnecessary. Moreover, the extent of normal potential ordering shrinks from 1.676 to 1.259 V upon going from singlet to triplet Fe^0 . It generally is predicted that ring-slipped 18- versus 20-electron species are more stable, but as Figure 1 demonstrates, this is not the case for Fe. As expected, high-spin Ru^0 and Os^0 states are prohibitively high in energy and play no role in electron-transfer thermodynamics. They have therefore been ignored in this study.⁵⁵

Disproportionation free energies, calculated as $\Delta \Delta G(\text{sol})'_{\text{disp}} = \Delta G(\text{sol})'_i - \Delta G(\text{sol})'_{\text{iv}}$, are +1.259, -0.059 , and -0.627 eV for **1**, **2**, and **3**, respectively, and compare well with the experimentally determined values of 1.20 and -0.03 eV for Fe and Ru and the large negative value estimated for Os. Why are these energies so different, and why do they change sign in the sequence Fe–Ru–Os? These are the key questions that govern the multielectron redox behavior. To answer them we examine the individual components of $\Delta \Delta G(\text{sol})'_{\text{disp}}$ utilizing the square scheme by dissecting it into the first $[\Delta G(\text{sol})'_i]$ and second $[\Delta G(\text{sol})'_{\text{iv}}]$ adiabatic electron-transfer energies and analyzing their attendant electronic and structural components. By insisting on no structural change along the horizontal lines in the diagram (except for step I_{SC}), we can interpret the energies on the horizontal lines as vertical electron attachment energies, that is, the intrinsic electronic energy that results from adding an electron to a molecular assembly.

Interestingly, there is a periodic trend in the first vertical electron attachment energies, labeled as 1i-a, 2i-a, and 3i-a. It becomes ~ 1 eV more unfavorable for each step down the triad: $\Delta G(\text{sol})'_{i-a} = -3.884$, -2.904 , and -2.023 eV for **1**, **2**, and **3**, respectively. This change in energy is consistent with the tendency of the 4d and 5d transition metals to bind more strongly to arene ligands.⁵² As a result, the metal-dominated, empty frontier orbitals that will serve as the electron-accepting orbitals are increasingly more M –L antibonding and consequently higher in energy. The MO diagrams of the $M(\text{hmb})_2^{2+}$ triad are compared in Figure 2. The redox-active orbital of these

d^6 systems is one of a degenerate $d_{xz,yz}$ antibonding pair, whose energy also increases by ~ 1 eV per metal. The more favorable electron attachment energy of $\text{Fe}(\text{hmb})_2^{2+}$ is therefore consistent with its weaker metal–arene bonding, and the highly unfavorable energy of the redox-active orbital in **3** explains why $\text{Os}(\text{hmb})_2^{2+}$ undergoes a hapticity change upon injection of only one electron: The redox-active orbital is so high in energy that its occupation generates an intermediate that undergoes structural rearrangement. The structural relaxation component of the first reduction is labeled as **1i-b**, **2i-b**, and **3i-b** in Figure 1. Consistent with the trends seen for the MOs, Os displays the largest structural reorganization energy of -0.908 eV, much larger than those for Fe and Ru, -0.180 and -0.214 eV, respectively. These structural relaxation energies compensate for some of the relatively unfavorable **3i-a** value discussed above, affording what we call the adiabatic free energy of reduction of -2.931 eV (**3i** in Figure 1) for $\text{Os}(\text{hmb})_2^{2+/+}$, which is similar to the -3.118 eV value that we compute for $\text{Ru}(\text{hmb})_2^{2+/+}$ (**2i** in Figure 1). The adiabatic free energy of reduction of $\text{Fe}(\text{hmb})_2^{2+/+}$ is much more negative, at -4.065 eV. Thus, two fundamentally different structural rearrangement responses are operative. The Fe and Ru complexes maintain the η^6 -coordination of both arene ligands and simply push the arene ligands farther away from the metal center in response to having one M–L antibonding orbital occupied. They form monocationic redox intermediates that are formally 19-electron species. This mild structural response to the redox stress is insufficient for the Os complex, as the M–L antibonding interaction is much stronger. It must undergo a more drastic structural change by invoking an $\eta^6 \rightarrow \eta^4$ hapticity change for one of the two arene ligands to afford a 17-electron cation, where the M–L antibonding interaction of the redox-active orbital can be minimized by lifting one edge of the arene ligand away from the metal center.

Whereas the first adiabatic free energy change becomes increasingly favorable in the sequence $\text{Os} < \text{Ru} < \text{Fe}$, the opposite trend is observed for the second reduction. Here, we compute -2.389 , -3.177 , and -3.558 eV for Fe, Ru, and Os, labeled as **1ii**, **2ii**, and **3ii**, respectively, in Figure 1. This trend is puzzling: Given the identical composition of the ligands and identical overall structural change upon reduction, it is plausible to expect at least a consistent trend for the first and second reductions. Judging from standard atomic electron affinities, the values of which become larger as we move from Fe to Ru to Os, we may naively have expected the electron attachment energy to become more negative in the sequence of Fe, Ru, and Os. But the analysis presented above emphasizes that deriving trend expectations for metal complexes from atomic behavior of transition metals can be deceptive.⁵³

The decisively negative second reduction free energy for Os is easy to understand. It derives largely from the much more favorable vertical electron attachment energy of -2.792 eV (step **3ii-a**), because this second reduction is now formally a $17e^- \rightarrow 18e^-$ versus a $19e^- \rightarrow 20e^-$ process. The accompanying structural relaxation, labeled as **3ii-b**, is consequently diminished for Os, at -0.767 eV, and is much smaller than the values calculated for Fe (-1.291 eV, **1ii-b**) and Ru (-1.609 eV, **2ii-b**). Larger structural relaxation energy for Ru is consistent with its greater need than Fe to relieve electronic stress by bending one hmb ligand and with its redox-active orbital being more antibonding in character. Despite the greater antibonding nature of the Ru redox active orbital, our calculations suggest that its second vertical attachment energy of -1.567 eV (step **2ii-a**) is

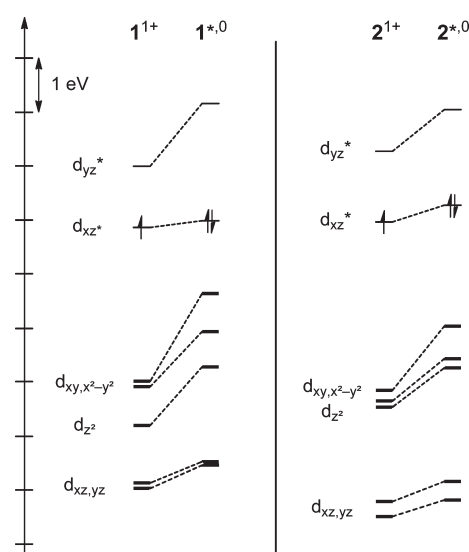


Figure 3. Orbital energy plots for the second vertical electron attachment in **1ii-a** (Fe) and **2ii-a** (Ru). Bold and regular lines correspond to doubly occupied and unoccupied orbitals, respectively, with electrons explicitly shown for the redox-active orbital. As described in the text, a background electrostatic term has been subtracted from the energies of the A^{*0} orbitals.

0.469 eV more negative than that of the Fe analogue, which shows a vertical electron attachment energy of -1.098 eV. This result is paradoxical: How can the redox-active orbital in the Ru complex, which is both more M–L antibonding and higher in energy than in the Fe case, accommodate the second electron with much less energy penalty? Given that the Ru complex undergoes a hapticity change, whereas the Fe complex does not, one is tempted to blame the differential structural distortion for such behavior. But this convenient explanation is false, as the discrepancy is found in the vertical electron attachment energy; i.e., there is no structural distortion energy included. To understand the origin of this paradoxical result, which lies at the center of the observed potential inversion and multielectron transfer in the Ru complex, we examined changes in the metal-based frontier orbital energies accompanying attachment of the second electron in more detail.

Orbital Energies. Figure 3 plots orbital energies for the monoreduced species 1^+ and 2^+ as well as those for the fully reduced species at the constrained ($1+$) geometries, which we denote 1^{*0} and 2^{*0} .⁵⁴ The dashed lines track the orbital energy shifts for these transformations that correspond to the second vertical electron attachment energies in Figure 1 (**1ii-a** and **2ii-a**). Unlike conventional orbital correlation diagrams, where the number of electrons is constant, the additional electron causes all orbital energies to increase in the reduced form, A^{*0} . To isolate important differences between the orbital energy penalties paid by the two species upon electron attachment, we must find a way of internally referencing the orbital energy changes. After much experimentation, we chose to use a spectator orbital on the hmb with no metal-based orbital character at any point of the redox process to establish a background Coulombic repulsion (ca. 3.65 eV), which increases the energy of all occupied orbitals simply due to the presence of the additional electron. By subtracting this term from the frontier orbital energies of 1^{*0} and 2^{*0} , shifts that are significantly larger than the background

electrostatic effect can be identified. These orbital energy differences are plotted in Figure 3.

There are two significant findings in the plots shown in Figure 3. First, the d_{xz} , d_{yz} and d_{xz}^* orbitals increase in energy more for Ru than for Fe. Because this effect is electrostatic in nature and dictated by the spatial extent of the orbital being occupied, it is reasonable to find that these Ru bonding orbitals experience a larger increase in energy due to their more covalent character than Fe. Indeed, maximum penalty in the bonding combination should arise at 50%–50% metal–ligand character due to optimum spatial overlap of the in- and out-of-phase orbitals, a feature we encountered previously in studying the redox chemistry of dinuclear, diamond core complexes of Mo and W.²⁷ If these were the only electronic effects operative, we would expect a normal ordering of reduction energies; i.e., the $\text{Fe}^{+/0}$ couple should display a more negative electron attachment energy than the $\text{Ru}^{+/0}$ couple, following the same rationale we utilized to justify the trend for the $\text{M}^{2+/+}$ couples above. The second, more important observation is that the nonbonding d_{z^2} , d_{xy} and $d_{x^2-y^2}$ orbitals of Fe experience an even larger increase in energy upon reduction, as highlighted in Figure 3. This larger electrostatic penalty ostensibly is due to the smaller size of the Fe ion, which causes its metal-based orbitals to be more sensitive to additional charge at the metal center. Furthermore, the weaker metal–arene bonding of Fe is less effective in dissipating charge into the hmb rings, leading to a more localized charge at the metal center in Fe compared to Ru.

As a net result, the addition of a second electron is highly unfavorable for the Fe complex compared to the Ru analogue, although the redox-active orbital is less M–L antibonding. The electrostatic penalty is less severe in the case of Ru, allowing the two vertical electron attachment energies 2i-a (–2.904 eV) and 2ii-a (–1.567 eV) to be much closer in energy, at 1.337 eV, than in the Fe sandwich, where the separation of the steps 1i-a (–3.884 eV) and 1ii-a (–1.098) is more significant, at 2.786 eV. The two vertical electron attachment energies of the Os complex should not be compared to those of the Fe and Ru complexes, as the molecular structures undergoing reduction are fundamentally different because the electron count is also different, as explained above. It is interesting to note, however, that the vertical electron attachment energies in the Os complex, –2.023 and –2.792 eV, respectively, are already inverted. For systems that undergo significant structural changes accompanied by redox events, it is common to assume that the character of the electrochemical response is mediated by or closely associated with the structural relaxation energy. Our analysis reveals that this common notion must be applied with some care for details, as it may lead to unproductive assumptions. For example, the observation that the Fe sandwich does not undergo a redox-triggered hapticity change, whereas the Ru and Os complexes do, may be interpreted as the structural relaxation associated with the hapticity change being critically important for the display of multielectron redox behavior. In this regard, it is interesting to examine the amount and distribution of structural relaxation energy for the three complexes examined: In the Os complex, the sum of the two structural relaxation energies 3i-b and 3ii-b is –1.675 eV, whereas –1.823 and –1.471 eV are found for the Ru and Fe complexes, respectively. Given that the Os complex is highly inverted, the Ru system is barely inverted, and the Fe sandwich shows highly classical potential ordering, these structural relaxation energies do not follow the redox trend. For any energy component to support or trigger potential inversion, the

most important feature is that the energy is apportioned unevenly between the first and second reduction steps. Specifically, the second reduction must be preferred energetically over the first to make the disproportionation of the cationic species more feasible. As our square diagram in Figure 1 illustrates, the opposite energy distribution is operative in this case: In the Fe complex, which shows the classical two-single-electron redox chemistry, the second step is associated with a structural relaxation energy of –1.291 eV (1ii-b) when only –0.180 eV (1i-b) is released in the first step. A very similar distribution of –1.609 vs –0.214 eV is found in the Ru complex. Thus, in both cases, the structural relaxation energies are very much inverted and contribute to pushing the equilibrium of $2(+1)$ vs $(+2) + (0)$ toward the disproportionated, right-hand side. In fact, this disproportionate distribution is an important feature for inverting the redox potentials of the Ru complex. Interestingly, the structural distortion energy of the Os complex, the most inverted system under consideration, is apportioned as to prefer a classical, noninverted scenario. The structural relaxation energy of the second step (3ii-b) is only –0.767 eV when the first step (3i-b) releases –0.908 eV, for reasons discussed above. Thus, the structural relaxation plays against the potential inversion in the case of Os.

In the reasoning outlined above, we used the hypothetical low-spin, singlet η^4 -isomer of $\text{Fe}(\text{hmb})_2^0$ in the electron-transfer sequence. Compared to singlet $\text{Fe}(\text{hmb})_2^0$, the triplet state lies 0.417 eV lower in energy (Figure 1).⁵⁵ In the triplet state, both arene rings retain η^6 binding, in agreement with experimental findings.^{56,57} If the singlet $\text{Fe}(\text{hmb})_2^0$ complex were the ground state, the redox potentials would be *more* normally ordered by ca. 0.4 V. Since the triplet state is computed to be the most realistic ground state of the neutral Fe complex, we must add the additional spin-crossover energy of –0.417 eV to the second step of the two-electron reduction. Whereas this additional term changes the extent of potential separation, it is too small to induce any meaningful difference neither in the logic of the arguments nor in the conceptual conclusions presented above.

CONCLUSIONS

In conclusion, the dramatic and apparently systematic transition from single to multiple electron transfer behavior in $\text{M}(\text{hmb})_2^{2+/+0}$ systems results from opposing periodic trends in the first and second electron attachment energies: the reduction free energy becomes less negative in the sequence Fe–Ru–Os for the first electron transfer, whereas it becomes more negative for the same sequence for the second electron attachment. As we noted previously,²⁷ decisive electronic energy changes in electron attachment processes of this magnitude often occur in lower-lying rather than frontier orbitals. Thus, a simple tracking of redox-active (LUMO/SOMO/HOMO) orbital energy changes based on Walsh's rule⁵⁸ is sometimes inadequate for a complete understanding of redox-triggered energy changes.

Despite the reasonable inference from experimental observations that a hapticity change leads to multielectron redox behavior, our analysis reveals that hapticity changes do not necessarily cause potential inversion. Instead, ring slippage and multielectron transfer arise from different electronic structure elements in the Fe triad with a more complex interplay than previously realized. Stronger bonding descending the periodic table controls the energetics of the first vertical electron attachment to the antibonding orbitals of $\text{M}(\text{hmb})_2^{2+}$ by ~ 1 eV per metal, with Fe being most favorable.

However, the first adiabatic electron attachment energies are calculated to be similar for Ru and Os, because a large structural relaxation in the form of a hapticity change accompanies the electron transfer at this stage. The energetics of the first electron transfer set the stage for apparent multielectron transfer in the two heavier metals, with Fe maintaining normally ordered events because of the overwhelming energy release in the first reduction. The extent of and the electronic cause of potential inversion in Ru and Os are found to be very different, with Ru exhibiting nearly overlapping one-electron steps and the Os potentials being inverted by 400 mV or more.¹⁵ This difference is traced through theoretical square schemes to the second vertical attachment energies, which go through different formal electron counts of $19e^- \rightarrow 20e^-$ for Ru and $17e^- \rightarrow 18e^-$ for Os. Thus, the timing of the hapticity change, which is a consequence of electronic structure, helps control the extent of potential inversion. Investigation of alternative spin-states for Fe also produces the counterintuitive finding that the thermodynamically more stable 20-electron $\eta^6:\eta^6 Fe^0$ triplet compresses the one-electron potentials by 400 mV compared with the ring-slipped $\eta^4:\eta^6$ singlet.

On the basis of our computational study, we can derive several insights for rational design of two-electron redox systems: In principle, first- and second-row transition metal complexes can be envisioned where (i) the first electron attachment energy for a second-row metal is so favorable that sequential one-electron events are observed and (ii) the first electron transfer of a first-row metal is so unfavorable that a subsequent spin-flip could overcome $\Delta\Delta G(\text{sol})'$ and drive multielectron behavior. Indeed, (i) was observed by Geiger and Weaver in their studies of $[\text{Cp}^*\text{Rh}(\text{hmb})]^{2+/\pm/0}$, wherein the odd-electron intermediate was experimentally observed, leading to the conclusion that the hapticity change accompanies the second electron transfer.¹⁹ Because the higher oxidation state of the metal center is not fully compensated for by the anionic Cp* ligand, the first electron attachment becomes favorable enough to shift the energetic balance between the first and second electron transfers toward stabilization of $[\text{Cp}^*\text{Rh}(\text{hmb})]^+$. The second objective (ii) of building a first-row metal capable of multielectron transfer would suggest moving toward a metal with a lower oxidation state and/or more-electron-rich ligands. Conceptual work toward this end is in progress in our laboratory.

■ ASSOCIATED CONTENT

Supporting Information. Cartesian coordinates of all complexes and computed energy components. This material is available free of charge via the Internet at <http://pubs.acs.org>.

■ AUTHOR INFORMATION

Corresponding Author
mbaik@indiana.edu

■ ACKNOWLEDGMENT

We thank the NSF (CHE-0645381, CHE-1001589 and 0116050) for financial support. M.-H.B. thanks the Research Corporation for the Cottrell Scholarship and the Scialog Award. R.L.L. thanks Allen Siedle for financial support through the Siedle Graduate Fellowship and Soumya Ghosh for fruitful discussions. M.-H.B. thanks Korea University for a visiting Professor appointment.

■ REFERENCES

- (1) Johnson, J. W.; Muetterties, E. L. *J. Am. Chem. Soc.* **1977**, *99*, 7395–7396.
- (2) Muetterties, E. L.; Bleeke, J. R. *Acc. Chem. Res.* **1979**, *12*, 324–331.
- (3) Muetterties, E. L.; Bleeke, J. R.; Wucherer, E. J.; Albright, T. A. *Chem. Rev.* **1982**, *82*, 499–525.
- (4) Pigge, F. C.; Coniglio, J. J. *Curr. Org. Chem.* **2001**, *5*, 757–784.
- (5) Dyson, P. J. *Dalton Trans.* **2003**, 2964–2974.
- (6) Rigby, J. H.; Kondratenkov, M. A. *Top. Organomet. Chem.* **2004**, *7*, 181–204.
- (7) Süß-Fink, G. *Dalton Trans.* **2010**, *39*, 1673–1688.
- (8) Pampaloni, G. *Coord. Chem. Rev.* **2010**, *254*, 402–419.
- (9) Finke, R. G.; Voegeli, R. H.; Langanis, E. D.; Boekelheide, V. *Organometallics* **1983**, *2*, 347–350.
- (10) Pierce, D. T.; Geiger, W. E. *J. Am. Chem. Soc.* **1989**, *111*, 7636–7638.
- (11) Pierce, D. T.; Geiger, W. E. *J. Am. Chem. Soc.* **1991**, *114*, 6063–6073.
- (12) Karpinski, Z. J.; Kochi, J. K. *J. Organomet. Chem.* **1992**, *437*, 211–225.
- (13) Bennett, M. A.; Bown, M.; Byrnes, M. J. *J. Organomet. Chem.* **1998**, *571*, 139–144.
- (14) Satou, T.; Takehara, K.; Hirakida, M.; Sakamoto, Y.; Takemura, H.; Miura, H.; Tomonou, M.; Shinmyozu, T. *J. Organomet. Chem.* **1999**, *577*, 58–68.
- (15) The general features of the voltammogram reported in ref 13 can be digitally simulated by successive one-electron transfers whose potentials are inverted by ~ 450 mV, assuming realistic values for the electron-transfer rate constants.
- (16) Koelle, U.; Fuss, B.; Rajasekharan, M. V.; Ramakrishna, B. L.; Ammeter, J. H.; Böhm, M. L. *J. Am. Chem. Soc.* **1984**, *106*, 4152–4160. Also in this work, $\text{Co}(\text{hmb})_2^{2+}$ exhibits normally ordered reductions separated by 2.28 V.
- (17) Bowyer, W. J.; Geiger, W. E. *J. Electroanal. Chem.* **1988**, *239*, 253–271.
- (18) Bowyer, W. J.; Geiger, W. E. *J. Am. Chem. Soc.* **1985**, *107*, 5657–5663.
- (19) Merkert, J.; Nielson, R. M.; Weaver, M. J.; Geiger, W. E. *J. Am. Chem. Soc.* **1989**, *111*, 7084–7087.
- (20) Nielson, R. M.; Weaver, M. J. *Organometallics* **1989**, *8*, 1636–1643.
- (21) (a) Neto, C. C.; Baer, C. D.; Chung, Y. K.; Sweigart, D. A. *J. Chem. Soc., Chem. Commun.* **1993**, 816–818. (b) Reingold, J. A.; Virkaitis, K. L.; Carpenter, G. B.; Sun, S.; Sweigart, D. A.; Czech, P. T.; Overly, K. R. *J. Am. Chem. Soc.* **2005**, *127*, 11146–11158. (c) Dai, W.; Kim, S. B.; Pike, R. D.; Cahill, C. L.; Sweigart, D. A. *Organometallics* **2010**, *29*, 5173–5178.
- (22) Baik, M.-H.; Ziegler, T.; Schauer, C. K. *J. Am. Chem. Soc.* **2000**, *122*, 9143–9154.
- (23) Baik, M.-H.; Schauer, C. K.; Ziegler, T. *J. Am. Chem. Soc.* **2002**, *124*, 11167–11181.
- (24) Yang, X.; Baik, M.-H. *J. Am. Chem. Soc.* **2006**, *128*, 7476–7485.
- (25) Yang, X.; Baik, M.-H. *J. Am. Chem. Soc.* **2008**, *130*, 16231–16240.
- (26) Schultz, F. A.; Lord, R. L.; Yang, X.; Baik, M.-H. *ACS Symp. Ser.* **2009**, *1012*, 151–166.
- (27) Lord, R. L.; Schultz, F. A.; Baik, M.-H. *Inorg. Chem.* **2010**, *49*, 4611–4619.
- (28) Evans, D. H. *Chem. Rev.* **2008**, *108*, 2113–2144.
- (29) Kraiya, C.; Evans, D. H. *J. Electroanal. Chem.* **2003**, *565*, 29–35.
- (30) Evans, D. H.; Busch, R. W. *J. Am. Chem. Soc.* **1982**, *104*, 5057–5062.
- (31) Baik, M.-H.; Friesner, R. A. *J. Phys. Chem. A* **2002**, *106*, 7407–7415.
- (32) *Jaguar 7.0*; Schrödinger LLC: New York, 2007.
- (33) Vosko, S. H.; Wilk, L.; Nusair, M. *Can. J. Phys.* **1980**, *58*, 1200–1211.
- (34) Lee, C. T.; Yang, W. T.; Parr, R. G. *Phys. Rev. B* **1988**, *37*, 785–789.

- (35) Becke, A. D. *Phys. Rev. A* **1988**, *38*, 3098–3100.
- (36) Becke, A. D. *J. Chem. Phys.* **1993**, *98*, 5648–5652.
- (37) Stephens, P. J.; Devlin, F. J.; Chabalowski, C. F.; Frisch, M. J. *J. Phys. Chem.* **1994**, *98*, 11623–11627.
- (38) Reiher, M.; Salomon, O.; Hess, B. A. *Theor. Chem. Acc.* **2001**, *107*, 48–55.
- (39) Hay, P. J.; Wadt, W. R. *J. Chem. Phys.* **1985**, *82*, 270–283.
- (40) Wadt, W. R.; Hay, P. J. *J. Chem. Phys.* **1985**, *82*, 284–298.
- (41) Hay, P. J.; Wadt, W. R. *J. Chem. Phys.* **1985**, *82*, 299–310.
- (42) Lord, R. L.; Schultz, F. A.; Baik, M.-H. *J. Am. Chem. Soc.* **2009**, *131*, 6189–6197.
- (43) Dunning, T. H., Jr. *J. Chem. Phys.* **1989**, *90*, 1007–1023.
- (44) Marten, B.; Kim, K.; Cortis, C.; Friesner, R. A.; Murphy, R. B.; Ringnalda, M. N.; Sitkoff, D.; Honig, B. *J. Phys. Chem.* **1996**, *100*, 11775–11788.
- (45) Edinger, S. R.; Cortis, C.; Shenkin, P. S.; Friesner, R. A. *J. Phys. Chem. B* **1997**, *101*, 1190–1197.
- (46) Rashin, A. A.; Honig, B. *J. Phys. Chem.* **1985**, *89*, 5588–5593.
- (47) Cramer, C. J. *Essentials of Computational Chemistry: Theories and Models*, 2nd ed.; J. Wiley: Hoboken, NJ, 2004.
- (48) Roy, L. E.; Jakubikova, E.; Guthrie, M. G.; Batista, E. R. *J. Phys. Chem. A* **2009**, *113*, 6745–6750.
- (49) Lord, R. L.; Schultz, F. A.; Baik, M.-H., unpublished data (see Appendix 1, Chapter 2 of R. L. Lord's Ph.D. thesis).
- (50) Only the gas-phase free energy change and solvation energy differences are included in Table 2. A detailed breakdown of these energies into their constituent parts is presented in the Supporting Information.
- (51) As found in our previous study employing this term,²⁷ $\Delta G(\text{sol})'$ is slightly better than $\Delta G(\text{sol})$ in matching experimentally determined potential orderings, whereas the opposite is true for absolute potentials.
- (52) Taube, H. *Coord. Chem. Rev.* **1978**, *26*, 33–45.
- (53) Richardson, D. E. *Inorg. Chem.* **1990**, *29*, 3213–3217.
- (54) To simplify the split α/β orbital diagram due to our use of an unrestricted formalism, we have averaged the α and β energies that correspond to the same spatial orbital.
- (55) Unsurprisingly, $\text{Ru}(\text{hmb})_2^0$ and $\text{Os}(\text{hmb})_2^0$ have high-energy triplet states, at 0.752 and 1.394 eV.
- (56) Michaud, P.; Mariot, J.-P.; Varret, F.; Astruc, D. *J. Chem. Soc., Chem. Commun.* **1982**, 1383–1385.
- (57) Rajasekharan, M. V.; Giezynski, S.; Ammeter, J. H.; Oswald, N.; Hamon, J. R.; Astruc, D.; Michaud, P. *J. Am. Chem. Soc.* **1982**, *104*, 2400–2407.
- (58) Albright, T. A.; Burdett, J. K.; Whangbo, M.-H. *Orbital Interactions in Chemistry*; John Wiley & Sons: New York, 1985.